

An Inverse Compton Scattering Origin of X-ray Flares from Sgr A*

F. Yusef-Zadeh¹, M. Wardle², K. Dodds-Eden³, C. O. Heinke⁴, S. Gillessen³, R. Genzel³, H. Bushouse⁵, N. Grosso⁶ & D. Porquet⁶

¹*Department of Physics and Astronomy, Northwestern University, Evanston, IL 60208*

²*Department of Physics and Astronomy, Macquarie University, Sydney NSW 2109, Australia*

³*Max Planck Institut für Extraterrestrische Physik, Postfach 1312, D-85741 Garching, Germany*

⁴*Dept. of Physics, University of Alberta, 4-183 CCIS, Edmonton AB T6G 2E1, Canada*

⁵*Space Telescope Science Institute, 3700 San Martin Drive, Baltimore, MD 21218*

⁶*Observatoire astronomique de Strasbourg, Université de Strasbourg, CNRS, INSU, 11 rue de l'Université, 67000 Strasbourg, France*

ABSTRACT

The X-ray and near-IR emission from Sgr A* is dominated by flaring, while a quiescent component dominates the emission at radio and sub-mm wavelengths. The spectral energy distribution of the quiescent emission from Sgr A* peaks at sub-mm wavelengths and is modeled as synchrotron radiation from a thermal population of electrons in the accretion flow, with electron temperatures ranging up to $\sim 5 - 20$ MeV. Here we investigate the mechanism by which X-ray flare emission is produced through the interaction of the quiescent and flaring components of Sgr A*. The X-ray flare emission has been interpreted as inverse Compton, self-synchrotron-Compton, or synchrotron emission. We present results of simultaneous X-ray and near-IR observations and show evidence that X-ray peak flare emission lags behind near-IR flare emission with a time delay ranging from a few to tens of minutes. Our Inverse Compton scattering modeling places constraints on the electron density and temperature distributions of the accretion flow and on the locations where flares are produced. In the context of this model, the strong X-ray counterparts to near-IR flares arising from the inner disk should show no significant time delay, whereas near-IR flares in the outer disk should show a broadened and delayed X-ray flare.

Subject headings: Galaxy: center - clouds - ISM: general - ISM - radio continuum - stars: formation

1. Introduction

Observations of stellar orbits in the proximity of the enigmatic radio source Sgr A*, located at the dynamical center of our galaxy, have shown compelling evidence that it is associated with a $4 \times 10^6 M_{\odot}$ black hole (Ghez et al. 2005; Gillessen et al. 2009; Reid and Brunthaler 2004). The extremely high spatial resolution made possible by its relative proximity provides the best laboratory for studying the properties of low-luminosity accreting black holes; $1''$ corresponds to 0.039 pc at the Galactic center distance of 8 kpc (Reid 1993). The emission from Sgr A* is assumed to be produced from radiatively inefficient accretion flow, as well as outflows. The bulk of the continuum flux from Sgr A* is considered to be generated in an accretion disk, where identifying the source of variable continuum emission becomes essential for our understanding of the launching and transport of energy in the nuclei of galaxies.

The emission from Sgr A* consists of both quiescent and variable components. The strongest variable component is detected as flares at near-IR and X-ray wavelengths (Baganoff et al. 2003; Genzel et al. 2003; Goldwurm et al. 2003; Eckart et al. 2006; Yusef-Zadeh et al. 2006a; Hornstein et al. 2007; Porquet et al. 2008; Dodds-Eden et al. 2009; Sabha et al. 2010; Trap et al. 2011), whereas only moderate flux variation is found at radio and sub-mm wavelengths (Falcke et al. 1998; Zhao et al. 2001; Herrnstein et al. 2004; Miyazaki et al. 2004; Yusef-Zadeh et al. 2006b; Marrone et al. 2008). The spectral energy distribution (SED) of the quiescent component peaks at sub-mm wavelengths and is identified in radio, millimeter and sub-mm wavelengths (see Genzel et al. 2010 and references therein). This emission is thought to be produced by synchrotron radiation from a thermal population of electrons with $kT \sim 10 - 30$ MeV participating in an accretion flow. A variety of models have been proposed to explain the quiescent emission from Sgr A* by fitting its SED, including a thin accretion disk, a disk and jet, an outflow, an advection-dominated accretion flow, a radiatively inefficient accretion flow, and advection-dominated inflow/outflow solutions (Blandford & Begelman 1999; Melia & Falcke 2001; Yuan et al. 2003; Liu et al. 2004; Genzel et al. 2011 and references cited therein). Unlike the quiescent component, which originates over a wide range of physical conditions and length scales of the accretion flow, flares are localized, allowing emission models to be directly tested with observations. As a supermassive black hole candidate, Sgr A* presents an unparalleled opportunity to closely study the process by which gas is captured, accreted, or ejected, by characterizing the emission variability over timescales of minutes to months. Because the time scale for variability is proportional to the mass of the black hole, this corresponds to variability on timescales 100 times longer than that of more massive black holes in the nuclei of other galaxies.

Studying near-IR emission from Sgr A* is crucial to track the acceleration of energetic

particles, as well as the accretion flow. Near-IR flares are produced by synchrotron radiation from a transient population of accelerated electrons. The near-IR emission is dominated by flaring activity that occurs a few times per day, with a small fraction of events showing simultaneous X-ray flares. The X-ray flare mechanism has been interpreted as either inverse Compton scattering (ICS), self-synchrotron-Compton (SSC), or synchrotron emission (Markoff et al. 2001; Liu & Melia 2002; Yuan et al. 2004; Yusef-Zadeh et al. 2006a; Eckart et al. 2009; Marrone et al. 2008; Dodds-Eden et al. 2009). The X-ray synchrotron mechanism implies that the acceleration mechanism must continuously resupply the 100 GeV electrons for the 30 minute duration of the observed flares, because the synchrotron loss time of the ~ 100 GeV electrons that are responsible for the synchrotron emission is ~ 30 seconds. The synchrotron self-Compton model requires that the local magnetic field be extremely large or that the number density of electrons is high. This is necessary to avoid overproducing the near-IR synchrotron emission from the large number of energetic electrons that are required to upscatter infrared photons into the X-ray band (Dodds-Eden et al. 2009; Marrone et al. 2008; Sabha et al. 2010; Trap et al 2011). The typical parameters of the magnetic field — $B \sim 1\text{-}10$ G or electron density $n_e \sim 10^9 \text{ cm}^{-3}$ — correspond to an energy density in the accelerated electrons a thousand times larger than that in the magnetic field. It is then difficult to understand how these particles are accelerated and confined.

In the case of X-ray emission produced by inverse Compton scattering, two possibilities have been explored. First, sub-mm photons arising from the quiescent component of Sgr A* may be upscattered by the transient electron population that is producing the IR synchrotron emission during IR flares (Yusef-Zadeh et al. 2006a). Alternatively, near-IR photons emitted during the flare may be upscattered by the mildly relativistic ~ 20 MeV electrons responsible for the quiescent radio–submm emission (Yusef-Zadeh et al. 2006a, 2008, 2009). If the sub-mm emission region were optically thin, this would produce a similar X-ray luminosity as the upscattering of sub-mm seed photons. However, because the sub-mm source is optically thick below ~ 1000 GHz, the observed sub-mm flux is produced by a fraction of the underlying electrons. The exact frequency at which the quiescent emission becomes optically thick is unknown. However, sub-mm measurements between 230 and 690 GHz (Marrone et al. 2006) indicate a flattening of the spectral index and thus a deviation from the rising spectrum observed at lower frequencies (An et al. 2005). The emission region is optically thin to near-IR photons, so all of these electrons are available to upscatter near-IR seed photons to X-ray energies (Yusef-Zadeh et al. 2009). The ICS luminosity produced through this scenario compares favorably with the observed near-IR and X-ray luminosities (Yusef-Zadeh et al. 2009). This is the model on which we will focus, as described below.

One of the predictions of the ICS model, in which near-IR photons are upscattered by $\sim 10 - 30$ MeV electrons, is a time delay between the peaks of the near-IR and X-ray flares

(Yusef-Zadeh et al. 2009; Dodds-Eden et al. 2009). Wardle (2011) provided the theoretical framework for the X-ray echo picture of the ICS. We present evidence for a time delay between the peaks of X-ray and near-IR flare emission based on seven new and archival observations. These measurements provide support for X-ray production via inverse-Compton scattering of IR flare photons by relativistic electrons of the accretion flow. The cross-correlation profiles of the peaks are generally skewed toward positive time lags, but show maximum likelihood values that have low signal-to-noise, due to the limited number of detections of simultaneous X-ray and near-IR flares.

2. Observations

2.1. X-rays

X-ray observations used in this study come from the Chandra observatory. Data obtained on July 6–7, 2004 and July 30, 2005 consist of 50.2 and 46 kilo-second (ks) observations, respectively, (ObsIDs 4683,5953), which were described previously by Eckart et al. (2006) and Munro et al. (2005). Data obtained in 2008 (not previously reported) consist of six 28 ks observations, starting May 5, May 6, May 10, May 11, July 25, and July 26 (ObsIDs 9169, 9170, 9171, 9172, 9174, 9173 respectively), scheduled to match nighttime IR observations in Chile (see below). All observations placed Sgr A* at the ACIS-I aimpoint and took data in FAINT mode.

We checked for any time intervals of strong background flaring (none were found) and then reprocessed the data using CIAO 4.3¹. This involved applying corrections to the energy scales to compensate for time-dependent gain changes and charge-transfer inefficiency, removing pixel randomization and improving spatial resolution, as well as creating an updated bad pixel map. We filtered the data for "bad" grades and status.

We extracted lightcurves (in spacecraft TT time) from a 1'' circular region around the position of Sgr A*, in the 1.5-8 keV energy range, using Gehrels (1986) errors. We converted the timestamps to UTC time following the prescription by A. Rots². The baseline quiescent X-ray emission from Sgr A* is spatially extended (Baganoff et al. 2003), but we see no variations in other local background emission. We tested several choices of binning the data for comparison to other wavelengths, settling on 1500 s binning for the 2008 data, 300 s binning for the major flare on 6–7 July 2004, and 600 s binning for the flare on July 30, 2005.

¹e.g. <http://cxc.harvard.edu/ciao/threads/createL2/>

²http://cxc.harvard.edu/contrib/arots/time_tutorial.html/

Using the absorbed thermal plasma model of Baganoff et al., the ratio of 1.5-8 keV counts to 2-10 keV unabsorbed flux is 8×10^{-11} ergs cm^{-2} s^{-1} per count/s. Recent measurements indicate a distance of 8.3 kpc to Sgr A* (Gillessen et al. 2009), but we assume a distance of 8 kpc, which gives $L_X(2-10) = 6 \times 10^{35}$ ergs/s per count/s, or a typical quiescent luminosity of 3×10^{33} ergs/s, in agreement with Baganoff et al. (2003).

We used Kolmogorov-Smirnov (K-S) tests (using the `lcstats` FTOOL³) on the 2008 Chandra lightcurves (binned to 32.41 s) to search for evidence of variability. We find evidence for variability in three of the 2008 observations, while another three show no evidence of variability. ObsIDs 9169, 9172, and 9173 give K-S probabilities of a constant lightcurve of 5×10^{-6} , 2×10^{-4} , and 1×10^{-8} , respectively, while the remaining observations give K-S probabilities greater than 5%. This significantly strengthens the evidence of variability from Sgr A* at very low levels, as Baganoff et al. (2003) reported a much larger K-S probability of constancy of 7×10^{-3} during quiescence. Given that the quiescent X-ray emission arises from much larger scales, presumably due to Bondi-Hoyle accretion (Baganoff et al. 2003), we suggest that the X-ray variability noted here is due to low-level flare emission superimposed on the steady quiescent emission. Alternatively, the X-ray variability on hourly time scales could arise from coronally active stars producing giant flares (Sazonov, Sunyaev and Revnivtsev 2011).

2.2. Near-IR

For the near-IR observations we use archival data taken with the VLT and HST. The near-IR data taken in 2004, 2005 and 2008 were observed with the near-IR adaptive optics-assisted imager NACO at the VLT (Lenzen et al. 2003; Rousset et al. 2003). We used Ks-band 13-milliarcsecond (mas) pixel imaging data from 2004 (nights of July 6-7) and 2005 (night of July 30-31) first presented by Eckart et al. (2006, 2008), and Ks-band 13-mas pixel polarimetric imaging data from 2008 (nights of May 4/5, 5/6, 9/10, 10/11 and July 25/26, 26/27) first presented in Dodds-Eden et al. (2011). We did not apply any data quality cut for the latter observations, except for the elimination of 11 images from July 25th, 2008, due to a bad AO correction (quadfoils, or a 'waffle' pattern).

We used both aperture photometry and PSF photometry methods to produce light curves, both carried out in the way described in Dodds-Eden et al. (2011). In particular we note that, for the purposes of that paper, the aperture method used two small apertures, one centered on the position of Sgr A* and the other on the star S17 (confused with Sgr

³<http://heasarc.gsfc.nasa.gov/lheasoft/ftools/xronos.html>

A* in 2006–2008), in order to measure their combined flux. Since S17 was further from Sgr A* in 2004 and the combined measurement of the flux is not important for the purposes of this paper, the use of the above method unnecessarily decreases the S/N. As a result, for the near-IR/X-ray comparison we supplemented the dataset with higher S/N light curves obtained from PSF photometry, though the data were sparsely sampled. We provide the light curve of S17 in the 2008 data set and the light curve of the comparison star S7 for the 2004 and 2005 data sets. The stellar background is estimated to be 3.4 ± 0.2 mJy in 2008 (Dodds-Eden et al. 2011).

Near-IR HST observations used in this study are NICMOS archival data obtained on 4 April 2007 as part of a larger Sgr A* monitoring campaign. Full observational details have been presented in Yusef-Zadeh et al. (2009). Briefly, the exposures used NICMOS camera 1, which has a pixel scale of $0.043''$, and the medium-band filters F170M and F145M, which have central wavelengths of 1.71 and $1.45 \mu\text{m}$, respectively, and FWHMs of $0.2 \mu\text{m}$. Individual exposures had a duration of 144 sec, with non-destructive detector readouts occurring every 16 sec. We averaged the readouts to sampling intervals of 64 and 128 seconds in the 1.71 and $1.45 \mu\text{m}$ bands, respectively, to obtain adequate S/N. Aperture photometry was performed on Sgr A* in each sampling interval, using an aperture diameter of 3 pixels in order to limit contamination by nearby stars.

All of the near-IR measurements presented here have been corrected for reddening using extinction values of $A_\lambda = 2.42$ ($2.2\mu\text{m}$), 4.34 ($1.71\mu\text{m}$), and 6.07 ($1.45\mu\text{m}$) from Fritz et al. (2011).

3. Results

The middle two panels of Figure 1 show the light curves from the archival Ks-band and X-ray observations of Sgr A* that were taken on 2005 July 30. The near-IR light curve of the comparison star S7 is shown in the top panel. The X-ray and near-IR light curves of Sgr A* were sampled at intervals of 200 and 600 s, respectively. These measurements, first reported in Eckart et al. (2008), indicate a flare with a peak X-ray luminosity of 8×10^{33} erg s^{-1} . The bottom panel shows the cross-correlation of these light curves. The cross-correlation analysis uses the Z-transformed discrete correlation function (ZDCF) algorithm (Alexander 1997). The ZDC function is an improved solution to the problem of investigating correlation in unevenly sampled light curves. Maximum likelihood values, as well as 1 and 2σ confidence intervals around those values are estimated using the start time of each bin. This analysis finds that the X-ray peak lags the near-IR peak in Figure 1 by ~ 8.0 (+10, -10.1) and 8.0 (+20.2, -17.9) minutes for 1 and 2σ maximum likelihood values, respectively. We varied

the sampling interval in the near-IR and X-ray data between 1.5 and 10 minutes, but the maximum likelihood lag value remained the same. Eckart et al. (2008) compared the X-ray and near-IR flare emission and found that the peaks are coincident within ± 7 minutes.

The aperture photometry technique that was used to reanalyze the near-IR VLT data from 2004 produced a light curve that is quite similar that published by Eckart et al. (2006), who deconvolved their images. The only difference is that the present analysis uses data extending up to 4h UT on July 7, which is longer than that of Eckart et al. (2006). The bottom three panels of Figure 2 show the cross-correlation of these near-IR and X-ray data with a maximum likelihood lag of 7.0 (+1.3, -1.1) minutes and (+7.5, -6.9) minutes with 1 and 2σ errors, respectively. The lag is larger than zero at the 1σ level. The near-IR light curve of the comparison star S7 is shown in the top panel. The light curve of S7 is constant and supports the variable emission from Sgr A* between 3 and 4h UT. The sampling of the near-IR data reduced using PSF photometry is much more sparse than the aperture photometry data. The 1σ cross-correlation peak using the PSF photometry showed a time lag 7.7 (+2.9, -3.4) minutes within the error bars of that reduced by aperture photometry. Eckart et al. (2006) also cross-correlated their data and showed no time delay within 10 minutes.

Next we examined the X-ray and near-IR light curves obtained on 2007 April 4 using XMM and VLT observations (flare #2 in Porquet et al. 2008; Dodds-Eden et al. 2009). These data contain the second brightest X-ray flare (flare #2 in Porquet et al; 2008) coincident with one of the strongest near-IR flares, that has ever been detected. The cross-correlation of the X-ray and near-IR data for this bright flare shows a 1σ maximum likelihood time delay of -0.5 (+7.0, -6.5) minutes, which is consistent with zero time delay (Dodds-Eden et al. 2009; Yusef-Zadeh et al. 2009). The peak luminosity of the brightest flare is 24.6×10^{34} erg s^{-1} (Porquet et al. 2008). Two other moderate X-ray flares (flares #4-5) were detected on 2004 April 4 following the bright X-ray flare. X-ray flares #4 and #5, with peak luminosities of $\sim 6 \times 10^{34}$ and $\sim 8.9 \times 10^{34}$ erg s^{-1} , respectively, are covered in the near-IR 1.71 and 1.45 μm NICMOS data. The cross-correlations of the X-ray and near-IR light curves for flares #4-5 are presented in Figure 3a-d. The NICMOS observations alternated between the 1.71 and 1.45 μm bands every 6 minutes. In all of the four cases studied, the maximum likelihood values of flares #4 and #5 show positive lags ranging between 5 and 10 minutes. Similar to the other cases analyzed here, the peaks of the cross-correlations are all skewed towards positive time lags.

Finally, we compared near-IR (VLT) and X-ray data taken in May and July 2008. Figure 4 shows the light curves from the two different days of observations. These X-ray flares are an order of magnitude less luminous than those detected in earlier observations. We have

carried out K–S tests indicating the reality of these low-level X-ray visibilities (§2.1). The cross-correlations of the light curves from these two days give maximum likelihood lags of 19 (+6.8, -2.4) and 14.6 (5.6, -2.9) minutes with 2σ error bars. Figure 4 also shows the cross-correlation of X-ray with near-IR light curves derived from PSF photometry. The resulting time delays of 26.5 (+19, -29) and 16.6 (14.8, -11.8) minutes are well within the error bars of the aperture photometry data. To provide additional support for the reality of the variability of Sgr A*, Figure 5 compares the light curves of Sgr A* and S17 using the 2008 May 5 and 2008 July 26 observations, which are based on PSF photometry. In these data, where Sgr A* and S17 are separated from each other, each source is detected independently.

Although most of the individual cross-correlation results that are presented here have low S/N, the 1σ maximum likelihood peaks in eight different measurements show a tendency for X-ray emission to lag near-IR emission rather than lead. The cross-correlation gives maximum likelihood near-IR-to-X-ray lag values that are systematically higher than zero. The strongest simultaneous near-IR and X-ray flares (Flare 2 in Porquet et al. 2008) do not show any time delay, whereas the faintest X-ray flares seem to show the longest time delays.

4. SSC Models

Several alternative models for the relationship between near-IR and X-ray flares have been proposed. Synchrotron emission from a high-energy tail of the accelerated electron population responsible for the near-IR flaring may be responsible for the observed X-ray flaring (Dodds-Eden et al. 2009, 2010). Self-synchrotron-Compton (SSC) models, in which the same population of electrons produce the near-IR synchrotron emission and upscatter lower-energy synchrotron photons, require an unrealistically compact, and hence over-pressured, source region (Dodds-Eden et al. 2009) or a very weak magnetic field or a high electron density to avoid overproducing the IR synchrotron emission (Marrone et al. 2008; Sabha et al. 2010; Trap et al. 2011).

In SSC models the observed ratio of the X-ray and IR fluxes demands a certain Thomson optical depth in relativistic electrons. SSC flare models (Marrone et al 2008; Sabha et al. 2010; Trap et al 2011) adopt source region radii R of order R_g . The requisite electron densities then imply a particular magnetic field strength, so that the synchrotron emission from the electron population matches the observed near-IR flaring. These SSC models have electron energy densities ranging between 10^3 and 2×10^5 times the magnetic energy density. Because electron acceleration mechanisms invoke magnetic fields, the energy density in the field should be comparable to or greater than the energy density of the accelerated particles. Thus, scaling the SSC models to equipartition fields by reducing the electron

density while increasing the magnetic field to keep the product $n_e B^{[(p+1)/2]}$ and hence the near-IR synchrotron flux fixed, one finds that a reduction in electron density by a factor of 40 or more is required. Thus, SSC contributes at most 1/40 of the observed X-ray flux in such a model.

Alternatively, one can attempt to construct SSC models in which the field is in equipartition by reducing the source size R , while keeping the products $n_e B^{[(p+1)/2]} R^3$ and $n_e R$ fixed to preserve the synchrotron and SSC fluxes, respectively. Equipartition between the relativistic electrons and magnetic field is attained when R is reduced by a factor of a thousand or more, with corresponding field strength in the $10^4 - 10^5$ G range, which is orders of magnitude more than what is reasonable.

5. X-ray Echo due to ICS

Here we focus on an inverse Compton scenario for the X-ray flares, suggested by Yusef-Zadeh et al. (2009) and outlined in more detail by Wardle (2011). In this model, near-IR flare photons are upscattered to X-ray energies by the thermal electrons ($kT_e \sim 10$ MeV) in the accretion flow. This process dominates the alternative inverse Compton pathway, in which the nonthermal energetic electrons responsible for the near-IR synchrotron emission upscatter sub-millimeter photons emitted by the thermal electrons in the accretion flow into the X-ray band (Rybicki & Lightman 1986, Chapter 7.5). This alternative ICS pathway is less effective because the accretion flow is optically thick in the sub-millimeter, so that the ratio between sub-mm photons and the thermal electrons producing them is reduced by a factor of the optical depth. Then the upscattering of near-IR photons proportionately produces more emission than would be inferred by implicitly assuming that the sub-millimeter synchrotron flux is optically thin (e.g. Dodds-Eden et al. 2009). In this process, the second order scattering echo can also produce MeV γ -ray emission with a luminosity L_γ that is lower than that of X-rays L_X by a factor of a few (ie $L_\gamma/L_X \sim L_X/L_{NIR}$).

One significant difference of the ICS picture from the synchrotron and SSC pictures is that the longer path from the near-IR source to the observer taken by an upscattered photon detected in the X-ray compared to the straight-line path taken by a photon received in the near-IR introduces a time delay between flaring in the near-IR and X-rays. In addition, because scattering occurs from a range of locations within the accretion flow, with a corresponding range of time delays, the reflection signal tends to be broadened compared to the near-IR seed photon light curve. While there is some evidence of systematic delays between the near-IR and X-ray flaring, the X-ray flares appear to generally have a narrow FWHM compared to their corresponding near-IR flares.

5.1. Modeling

To explore whether this model can plausibly explain the X-ray flaring, we compute the X-ray “echoes” of the observed near-IR flares to compare with our simultaneous X-ray observations. We make a number of simplifying assumptions, none of which are severe. We assume that the observed near-IR flare comes from a point located in the accretion flow with a power-law spectrum and Gaussian light curve, $S_\nu(t) \propto \nu^{-0.5} \exp(-(t - t_0)^2/2\sigma^2)$. Because the X-ray flares are narrower than the near-IR we have assumed that the FWHM of the near-IR flaring narrows as $\lambda^{0.5}$ below $2.2 \mu\text{m}$. The physical justification is that the synchrotron loss time scale scales as $\lambda^{0.5}$ and becomes comparable with the observed FWHM at about $2 \mu\text{m}$. The energy of an upscattered photon with initial energy $h\nu_{\text{IR}}$ is assumed to be $\frac{4}{3}\gamma^2 h\nu_{\text{IR}}$ where γ is the electron Lorentz factor. Because the upscattered photon energies are much lower than the electron rest energy, the scattering occurs in the Thompson regime. Assuming isotropic upscattering, the total production rate of upscattered photons per unit volume is $n_{\text{IR}}n_e\sigma_{TC}$, where n_{IR} and n_e are the number densities of infrared photons and relativistic electrons, respectively. We ignore relativistic effects such as the Doppler boosting associated with the bulk motion of the accretion flow, because the corresponding Lorentz factor is small compared to that of the individual electrons. We also ignore the time delay, gravitational redshift and lensing effects of the Kerr metric, which only become important close to the event horizon in highly inclined systems.

The electron density and temperature profiles in the accretion flow are assumed to be steady, axisymmetric power-laws in cylindrical radius r , with $n_e \propto r^{-0.75}$ and $T_e \propto r^{-1}$ and the density truncated within $2 R_g$ and beyond $20 R_g$. The accretion flow is assumed to be confined to a thick disk with scale height/radius $(h/r) = 0.5$. The electron population is characterized by an approximate relativistic Maxwellian $f(x) = 1/2 x^2 \exp(-x)$, where $x = E/(kT_e)$, which is a good approximation for $kT_e \gtrsim 2 \text{MeV}$. The adopted profiles are within the typical ranges considered in analytic estimates (e.g. Loeb & Waxman 2007), semi-analytic models for the accretion flow (e.g. Yuan, Quataert & Narayan 2003), and MHD simulations (e.g. Mościbrodzka et al. 2009).

The remaining parameters specify the flare location relative to the line of sight and relative to the accretion flow: the inclination i of the disk to the line of sight, and the flare location (r, ϕ, z) in the natural cylindrical coordinate system. The low optical depth of the accretion flow to near-IR photons means that the results are insensitive to the inclination i and the azimuthal angle ϕ between the flare location and the poloidal plane containing the line of sight and the z-axis. We therefore fix these at typical values $i = 45^\circ$ and $\phi = 90^\circ$, respectively. Similarly, the results are insensitive to the height z of the near-IR flare for $z \lesssim r$, so we simply assume that the flare occurs in the disk midplane, ie. that $z = 0$.

The free parameters are the electron density n_0 and temperature T_0 at the fiducial radius 2×10^{12} cm, and the radial location of the flare, r . The noisiness of the observed light curves preclude formal fitting, so for each near-IR/X-ray flare combination we adjust these parameters by hand to approximately match the X-ray light curve. Reasonable matches to the observed X-ray profile are obtained with flares occurring at $r \sim 10R_s$, and electron densities $\sim 10^{7.5}-10^{8.5} \text{ cm}^{-3}$ and temperatures $\sim 5-20 \text{ MeV}$, as listed in Table 1.

In the context of the ICS picture, we fit a sample of light curves that have good time coverage in near-IR and X-ray wavelengths in order to illustrate the point that this model can potentially be a powerful tool to quantify the physical characteristics of the accretion flow. The light curves presented in Figures 1 and 2 are modeled following the second brightest X-ray flare that has ever been recorded on 2007 April 4 (Porquet et al. 2008). The light curves of the moderate flare that followed this bright flare (flare #2) is presented in Figure 3. The time delays of the peak emission shown in Figures 1, 2 and 3 are 8, 7 and 8 minutes, respectively, whereas the bright flare on 2007 April 4 showed a time delay consistent with zero. Given the limited simultaneous time coverage of the flares shown in Figure 3 and 4, we focus only on modeling these four flares. Figure 6 shows the observed and modeled light curves for the simultaneous near-IR and X-ray flares that occurred on 2005 July 30, 2004 July 6/7 and 2007 April 04 (the main flare and flare #4). Parameters of the fit for each of the four examples are shown in Table 1. Substructures corresponding to two weak flares in Figure 6a are also modeled with the same parameters as the main flare, as listed in Table 1. A baseline level has been subtracted from the near-IR light curves before constructing the theoretical light curves. If we restrict the evaluation of χ^2 to just the flare part of the X-ray light curve, χ^2/df is between 3–4. The reason is that there is often point-to-point variability in the light curve that throws points well away from the smooth "prediction". In addition, the near-IR light curve in Figure 6c shows substructures that could be arising from different flares, which would have different time delays in the context of ICS. Thus we have not formally fit the light curves as our models are illustrative only. Given these limitations, we obtain reasonable parameters from the theoretical X-ray light curves, which are superimposed on the observed light curves in Figure 6.

In each case a Gaussian form of the near-IR light curve has been adopted to represent the observed (extinction-corrected) near-IR flare at $3.8 \mu\text{m}$, $2.2 \mu\text{m}$ and $1.7 \mu\text{m}$. However, in our models, the X-ray flare arises from scattered optical photons. We assume the peak flux of the synchrotron flare (emitting at near-IR to optical) scales as $\nu^{-0.5}$ with frequency. Because the X-ray flare is narrower than the near-IR we have assumed that the FWHM is constant below $2.2 \mu\text{m}$ and narrows as $\lambda^{0.5}$ shortward of this. Reasonable matches to the observed X-ray profile are obtained with the flare occurring at the inner edge of the density profile and electron densities, as their estimated values are given in Table 1. The FWHM assumption

requires both the rise and the decay timescale of the flare to be faster at optical frequencies than at near-IR. For the decay timescale, this is a natural result of synchrotron cooling (the synchrotron loss time scale scales as $\nu^{-0.5}$). The rise time scale depends on the acceleration mechanism. While the acceleration mechanism of flare production is not understood, it is plausible that optically-emitting electrons are produced later than IR-emitting electrons (Kusunose and Takahara 2011).

Another issue involves the prediction that the spectral index between X-rays and near-IR/optical emission be identical in the context of ICS with the assumption that the electron distribution has a single power law spectrum. It is, however, possible that the energy spectrum of electrons has a broken power-law, thus producing a different spectral index in near-IR and X-rays. The mismatch in spectral index is in fact noted for the bright X-ray flare coincident with a strong near-IR flare of 2007 April 4 (Dodds-Eden et al. 2009). Although these authors discuss the difference in the spectral index using a synchrotron mechanism, the broken power law of NIR emitting electrons with a steeper spectral index shortward of $3.8\mu\text{m}$ was also argued in the ICS scenario (Yusef-Zadeh et al. 2009).

Although the spectral index measurements in X-ray and near-IR can not distinguish between the synchrotron and ICS models for the production of X-rays, it is predicted that the ratio of near-IR to X-ray flare emission can increase with increasing time delay in the ICS scenario. This is because bright X-ray flares are generated in the inner disk where the time delay is expected to be small. Although the available data are limited to test this aspect of the proposed model, we note a trend that is consistent with this expectation. Table 2 shows the ratio of $2.2\mu\text{m}$ peak flux (mJy) to peak X-ray luminosity ($10^{35}\text{ erg s}^{-1}$) for seven different measurements. The 1σ error bars of the maximum likelihood values are given in column 7. The smallest to largest flux ratios, as shown in column 6 of Table 2, support the trend that near-IR/X-ray flux ratios increase with the time delay, as expected in the context of the ICS model. For the near-IR observations on 2007 April 4 obtained at 3.8 and $1.7\mu\text{m}$, we convert the peak flux to $2.2\mu\text{m}$ using the spectral index of -0.7 , where $S_\nu \propto \nu^{-0.7}$, before we estimate the flux ratio. Future simultaneous measurements of X-ray and near-IR flares should examine the correlation of the peak near-IR to X-ray flux as a function of increasing observed time delay.

In summary, we have presented cross-correlations of simultaneous X-ray and near-IR flare light curves from Sgr A* and found a time lag of the X-ray peak flare emission with respect to the near-IR. Such an X-ray echo provides support for inverse Compton scattering of near-IR flare photons by $\sim 5 - 20\text{ MeV}$ electrons. A fraction of near-IR flare photons must upscatter from the accretion flow into the X-ray band. This can be significant for plausible accretion models, and therefore may explain the observed X-ray flares, or at least

Table 1. Model Parameters for Flare Events

Flare	kT_0^a (MeV)	n_0^b (cm ⁻³)	r^c (cm)
2004 Jul 07	9	2.9×10^8	1.0×10^{13}
2005 Jul 30	20	2.3×10^7	1.0×10^{13}
2007 Apr 04 #2	7	2.1×10^8	4.0×10^{12}
2007 Apr 04 #4	5	7.9×10^8	1.0×10^{13}

^aAccretion flow temperature profile $T_e(r) = T_0(r/r_0)^{-1}$
 where $r_0 = 2 \times 10^{12}$ cm

^bDensity profile $n_e(r, z) = n_0(r/r_0)^{0.75} \exp(-2z^2/r^2)$

^cRadial location of near-IR flare in equatorial plane.
 ($R_s \approx 1.2 \times 10^{12}$ cm for $M_{\text{BH}} = 4 \times 10^6 M_\odot$)

Table 2. Flux Ratios vs. Time Delay

Flare	IR backg.	X-ray backg.	IR peak mJy	X-ray Peak 1×10^{35} erg s ⁻¹	Peak Ratio IR/X-ray	Time Delay (minutes 1σ)
2007 Apr 04 #2	5.0	0.2	16.5	4.8	3.4	-0.5 (+7, -6.5)
2007 Apr 04 #5	-0.2	0.2	2.63	1.23	2.1	5.0 (+1.9, -1.5)
2007 Apr 04 #4	-0.2	0.2	4.67	1.22	3.8	5.0 (+1, -1.4)
2004 Jul 07	1.5	0.03	6	0.39	15.5	7 (+1.3 -1.2)
2005 Jul 30	0.0	0.002	5.9	0.13	45.4	8 (+10, -10.1)
2008 July 26+27	5.5	0.003	3.7	0.05	68.5	14.6 (+5.6, -7.4)
2008 May 5	6	0.003	2.74	0.021	130.0	19 (+6.8, -2.4)

place significant constraints on the accretion flow. Future cross-correlations based on more continuous near-IR and X-ray observations should give us better S/N in the maximum likelihood values of the time lag. In the context of the ICS model, future measurements will place better constraints on the density and temperature profiles of the accretion flow and the location of near-IR flares.

This work is partially supported by grants AST-0807400 from the National Science Foundation and DP0986386 from the Australian Research Council. COH is supported by NSERC and an Ingenuity New Faculty Award.

REFERENCES

- Alexander, T. 1997, *MNRAS* 285, 891
- An, T., Goss, W. M., Zhao, J.-H., Hong, X. Y., Roy, S., Rao, A. P., and Shen, Z.-Q. 2005, *ApJ*, 634, L49
- Baganoff, F. K., et al. 2003, *ApJ*, 591, 891
- Blandford, R. D. and Begelman, M. C. 1999, *MNRAS*, 303, L1
- Dodds-Eden, K., Porquet, D., Trap, G., Quataert, E., Haubois, X., Gillessen, S., Grosso, N., Pantin, E., Falcke, H., Rouan, D., Genzel, R., Hasinger, G., Goldwurm, A., Yusef-Zadeh, F., Clenet, Y., Trippe, S., Lagage, P.-O., Bartko, H., Eisenhauer, F., Ott, T., Paumard, T., Perrin, G., Yuan, F., Fritz, T. K. & Mascetti, L. 2009, *ApJ*, 698, 676
- Dodds-Eden, K., Sharma, P., Quataert, E., Genzel, R., Gillessen, S., Eisenhauer, F., & Porquet, D. 2010, *ApJ*, 725, 450
- Dodds-Eden, K., et al. 2011, *ApJ*, 728, 37
- Eckart, A., Baganoff, F. K., Schödel, R., Morris, M., Genzel, R., Bower, G. C., Marrone, D., Moran, J. M., Viehmann, T., Bautz, M. W., Brandt, W. N., Garmire, G. P., Ott, T., Trippe, S., Ricker, G. R., Straubmeier, C., Roberts, D. A., Yusef-Zadeh, F., Zhao, J. H., & Rao, R. 2006, *A&A*, 450, 535
- Eckart, A., et al. 2008, *A&A*, 492, 337
- Eckart, A., et al. 2009, *A&A*, 500, 935

- Fritz, T. K. et al. 2011, in press
- Gehrels, N. 1986, ApJ, 303, 336
- Genzel, R., Eisenhauer, F., & Gillessen, S. 2010, Reviews of Modern Physics, 82, 3121
- Genzel, R., Schödel, R., Ott, T., Eckart, A., Alexander, T., Lacombe, F., Rouan, D., and Aschenbach, B., 2003, Nature, 425, 934
- Ghez, A. M., Salim, S., Hornstein, S. D., Tanner, A., Lu, J. R., Morris, M., Becklin, E. E., & Duchêne, G. 2005, ApJ, 620, 744
- Gillessen, S., Eisenhauer, F., Trippe, S., Alexander, T., Genzel, R., Martins, F., & Ott, T. 2009, ApJ, 692, 1075
- Goldwurm, A., Brion, E., Goldoni, P., Ferrando, P., Daigne, F., Decourchelle, A., Warwick, R. S., and Predehl, P. 2003, ApJ, 584, 751
- Herrnstein, R. M., Zhao, J.-H., Bower, G. C., and Goss, W. M. , 2004, ApJ, 127, 3399
- Hornstein, S. D., Matthews, K., Ghez, A. M., Lu, J. R., Morris, M., Becklin, E. E., Rafelski, M., & Baganoff, F. K. 2007, ApJ, 667, 900
- Kusunose, M. & Takahara, F. 2011, ApJ, 726, 54
- Lenzen, R. et al. 22003, Proc. SPIE, 4841, 944
- Liu, S. and Melia, F. 2002, ApJ, 566, L77
- Liu, S., Petrosian, V., & Melia, F. 2004, ApJ, 611, L101
- Loeb, A., & Waxman, E. 2007, J. Cosmology Astropart. Phys., 3, 11
- Markoff, S., Falcke, H., Yuan, F., and Biermann, P. L. 2001, A&A, 379, L13
- Marrone, D. P., Moran, J. M., Zhao, J.-H., and Rao, R. 2006, Journal of Physics Conference Series, 54, 354
- Marrone, D. P., Baganoff, F. K., Morris, M. R., Moran, J. M., Ghez, A. M., Hornstein, S. D., et al. 2008, ApJ, 682, 373
- Melia, F. & Falcke, H. 2001, ARA&A, 39, 309
- Miyazaki, A., Tsutsumi, T., and Tsuboi, M., 2004, ApJ, 611, L97

- Muno, M. et al. 2005, *ApJ*, 633, 228
- Mosćibrodzka, M., Gammie, C. F., Dolence, J. C., Shiokawa, H. & Leung, P. K. 2009, *ApJ*, 706, 497
- Porquet, D., Grosso, N., Predehl, P., Hasinger, G., Yusef-Zadeh, F., Aschenbach, B., Trap, G., Melia, F., Warwick, R. S., Goldwurm, A., Bélanger, G., Tanaka, Y., Genzel, R., Dodds-Eden, K., Sakano, M., & Ferrando, P. 2008, *A&A*, 488, 549
- Reid, M. J. 1993, *ARAA*, 31, 345
- Reid, M. J., & Brunthaler, A. 2004, *ApJ*, 616, 872
- Rousset, G., et al. 2003, *Proc. SPIE*, 4839, 140
- Rybicki, G. B. & Lightman, Alan P. 1986, Chapter 7.5, *Radiative Processes in Astrophysics*, ISBN 0-471-82759-2. Wiley-VCH
- Sabha, N., Witzel, G., Eckart, A., Buchholz, R. M., Bremer, M., Gießübel, R., et al. 2010, *A&A*, 512, A2
- Sazonov, S., Sunyaev, R., and Revnivtsev, M. 2011, *ArXiv e-prints* (1108.2778)
- Trap, G., Goldwurm, A., Dodds-Eden, K., Weiss, A., Terrier, R., Ponti, G., et al. 2011, *A&A*, 528, A140
- Wardle, M. 2011, *Astronomical Society of the Pacific Conference Series*, 439, 450
- Yuan, F., Quataert, E., & Narayan, R. 2003, *ApJ*, 598, 301
- Yuan, F., Quataert, E., and Narayan, R. 2004, *ApJ*, 606, 894
- Yusef-Zadeh, F., et al. 2006a, *ApJ*, 644, 198
- Yusef-Zadeh, F., Bushouse, H., Wardle, M., Heinke, C., Roberts, D. A., et al. 2009, *ApJ*, 706, 706
- Yusef-Zadeh, F., Roberts, D., Wardle, M., Heinke, C. O., and Bower, G. C., 2006b, *ApJ*, 650, 189
- Zhao, J.-H., Bower, G. C., and Goss, W. M. 2001, *ApJ*, 547, L29

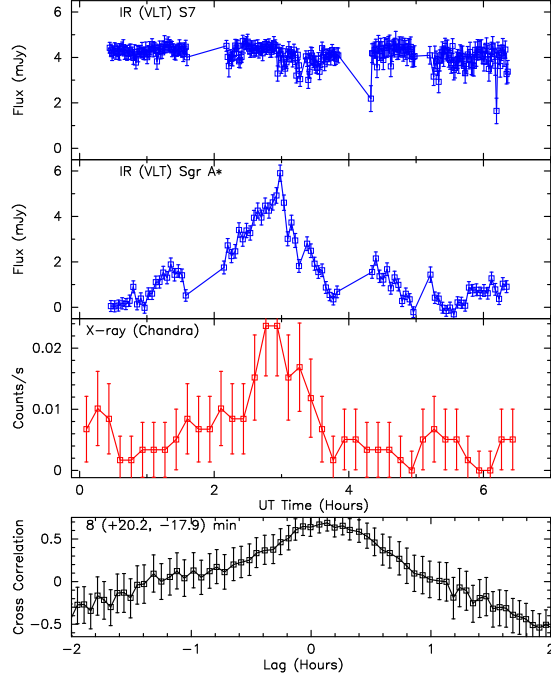


Fig. 1.— The light curve of the comparison star S7 is shown in the top panel with a time sampling of 65 sec. Two middle panels show the light curves of Ks-band ($2.2\mu\text{m}$) and X-ray (2-8keV) data taken simultaneously by the VLT and Chandra on 2005 July 30 (Eckart et al. 2008). The time sampling for the X-ray and near-IR data are 600 and 200 seconds, respectively. The cross correlation of the lightcurves and the corresponding 2σ maximum likelihood values are shown in the bottom panel. The 1σ error bar is given in Table 2. A base level of 4.2 mJy have been subtracted from the lightcurve of Sgr A* (Dodds-Eden et al. 2011).

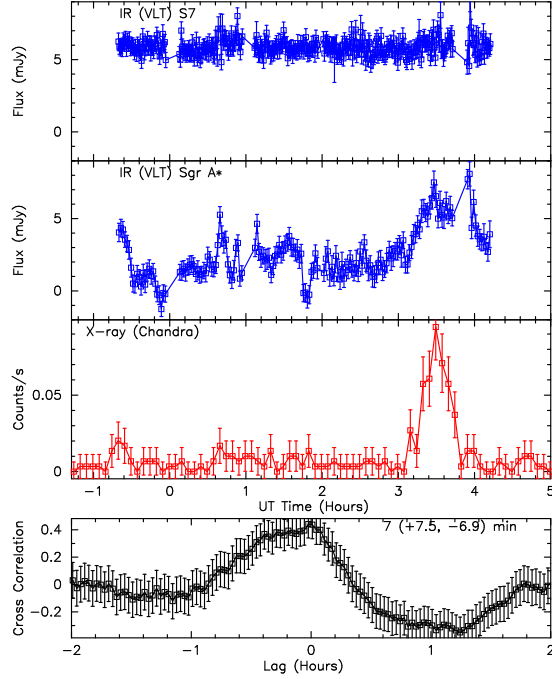


Fig. 2.— The top panel shows K-band ($2.2\mu\text{m}$) VLT data of the comparison star on S7 with a time sampling of 45 seconds and Sgr A* on 2004 July 6/7, while the third panel shows simultaneous Chandra X-ray (2-8 keV) data (Eckart et al. 2006). The middle two panels show the light curves of K-band ($2.2\mu\text{m}$) and X-ray (2-8 keV) data taken simultaneously by the VLT and Chandra on 2004 July 6/7 (Eckart et al. 2006). The time sampling for the X-ray and near-IR data on Sgr A* are 300 and 140 seconds, respectively. The cross correlation of the lightcurves is plotted in the bottom panel. For the 2004 lightcurve determined from aperture photometry the stellar background estimate is 5.3 ± 0.2 mJy which has been subtracted. For the lightcurve determined from PSF photometry (separated from S17 and S19 and free from any contribution from the seeing halo of S2) the specific amount of faint stellar contribution is not clear, but small, < 1 mJy. A maximum likelihood value with 2σ error bars are shown in the bottom panel. The 1σ error bar is given in Table 2.

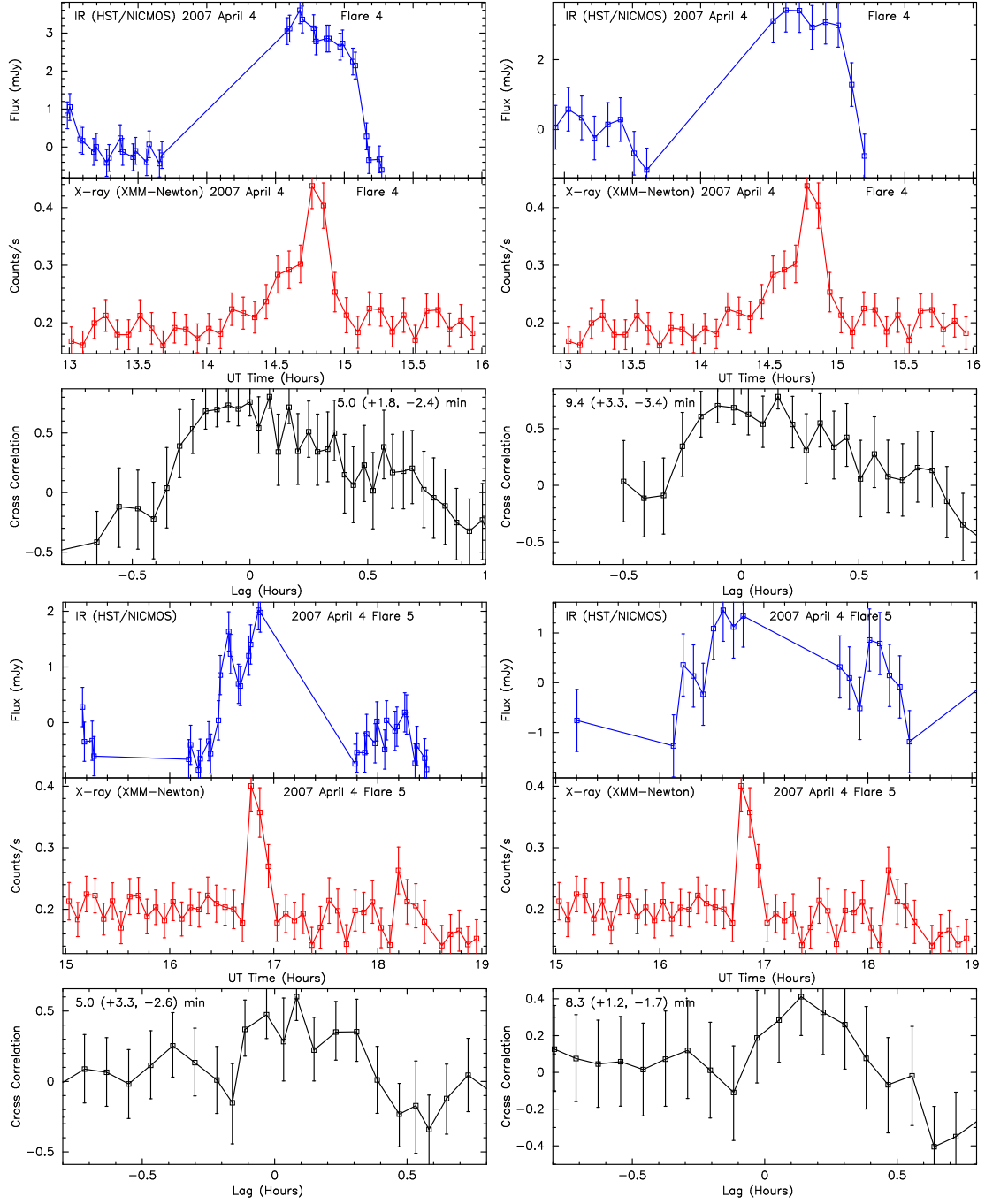


Fig. 3.— (a - Top Left) The light curves of flare #4 of 2007 April 4 in near-IR ($1.70\mu\text{m}$) and X-ray (2-10 keV) are taken by HST/NICMOS, and XMM/EPIC, with time sampling of 64 and 300 seconds, respectively. (b - Top Right) The same as (a) except that the $1.45\mu\text{m}$ are sampled at 144 second interval to improve the S/N. (c - Bottom Left) The same as (a) except that the light curves of flare # 5 are displayed at $1.70\mu\text{m}$. (d - Bottom Right) The same as (b) except that the light curves of flare # 5 are displayed at $1.45\mu\text{m}$. The cross correlation and the maximum likelihood values with 2σ error bars are shown in bottom panels. The 1σ error bars for flares #4 and 5 at $1.70\mu\text{m}$ are given in Table 2.

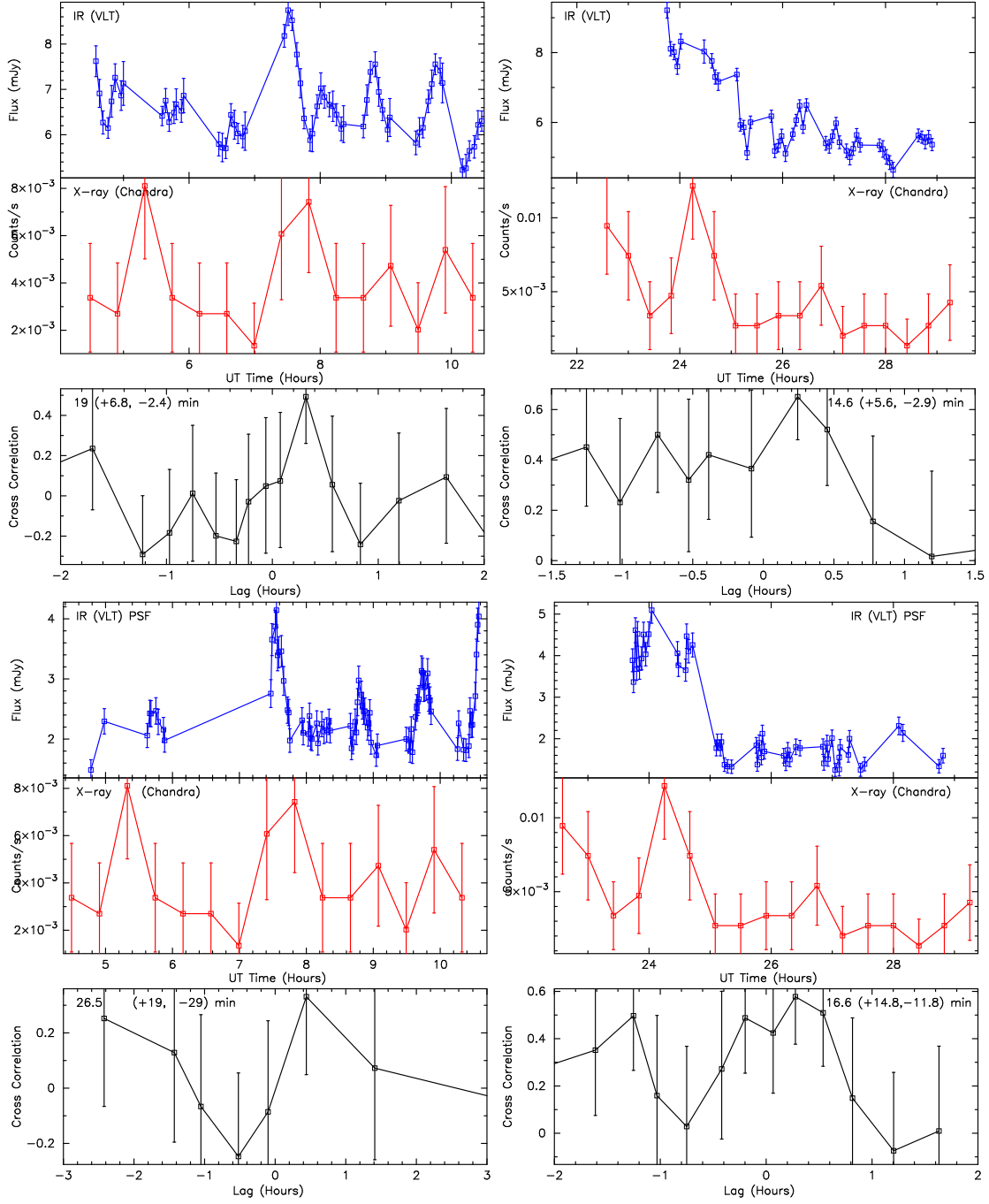


Fig. 4.— (a - Top Left) Using aperture photometry technique, top two panels show the light curves of Ks-band ($2.2\mu\text{m}$) and X-ray (2-8keV) data taken simultaneously with VLT and Chandra on 2008 May 5. The sampling interval for X-ray and near-IR data are 25 and ~ 2 minutes, respectively. The cross correlation of the light curves is plotted in the bottom panel. (b - Top Right) Similar to (a) except that the data taken on 2008, July 26+27. (c - Bottom Left) Similar to (a) except the light curve of Sgr A* is calibrated using PSF photometry technique. (d - Bottom Right) Similar to (b) except the light curve of Sgr A* is calibrated using PSF photometry technique. The cross correlation and the maximum likelihood values with 2σ error bars are shown in bottom panels. The 1σ error bars for aperture photometric data are given in Table 2.

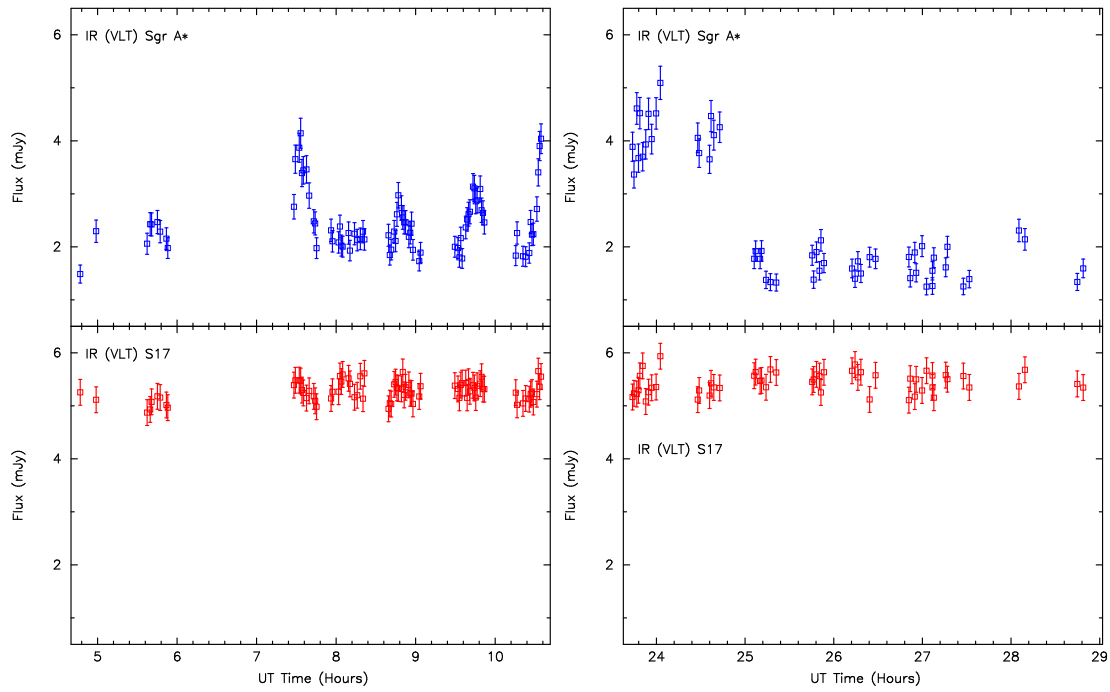


Fig. 5.— (a - Left) Top two panels show the light curves of PSF photometrically reduced Sgr A* and S17 at $2.2\mu\text{m}$ on 2008 May 5. (b - Right) Similar to (a) except that the data taken on 2008, July 26+27. A base level of 3.6 mJy has been subtracted.

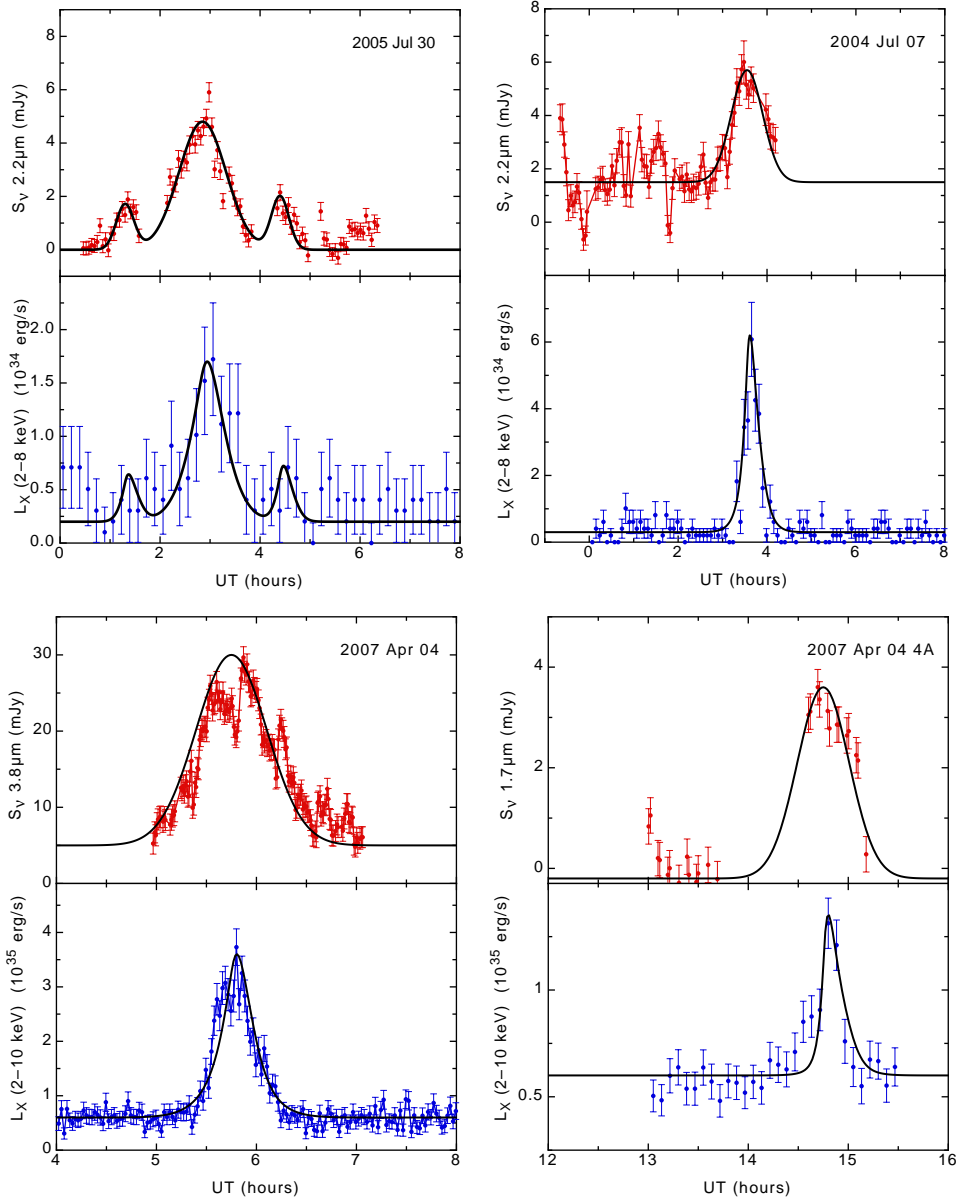


Fig. 6.— Adopted near-IR light curves and the corresponding ICS produced X-ray light curves (solid lines) superimposed on the near-IR and X-ray flares observed on 2005 July 30 (Top Left), 2004 July 7 (Top Right), and two flares on 2007, April 4 (Bottom Left and Right), respectively. Near-IR flare data are an input to the ICS model. The X-ray and near-IR flare of 2005 July 30 and 2004 July 7 are taken from Eckart et al. (2006, 2008) whereas the 2007, April 4 data are taken from Porquet et al. (2008) and Dodds-Eden et al. (2009). The ICS model parameters are listed in Table 1. Two weak flares before and after the main flare in the 2005 data in (a) have also been modeled. The A possible second flare of the 2004 data near 4h UT, as shown in Figure 2, has not been modeled in (b).